Assessing the significance of fidelity as a figure of merit in quantum state reconstruction of discrete and continuous variable systems

Antonio Mandarino,[1] Matteo Bina,[1] Carmen Porto,[1] Simone Cialdi,[1,2] Stefano Olivares,[1,2] and Matteo G. A. Paris[1,2]

[1]*Dipartimento di Fisica, Università degli Studi di Milano, I-20133 Milano, Italy*
[2]*Istituto Nazionale di Fisica Nucleare, Sezione di Milano, I-20133 Milan, Italy*

(Dated: April 4, 2016)

We experimentally address the significance of fidelity as a figure of merit in quantum state reconstruction of discrete (DV) and continuous variable (CV) quantum optical systems. In particular, we analyze the use of fidelity in quantum homodyne tomography of CV states and maximum-likelihood polarization tomography of DV ones, focussing attention on nonclassicality, entanglement and quantum discord as a function of fidelity to a target state. Our findings show that high values of fidelity, despite well quantifying geometrical proximity in the Hilbert space, may be obtained for states displaying opposite physical properties, e.g. quantum or semiclassical features. In particular, we analyze in details the quantum-to-classical transition for squeezed thermal states of a single-mode optical system and for Werner states of a two-photon polarization qubit system.

PACS numbers: 03.65.Ta, 42.50.Dv

arXiv:1604.00313v1 [quant-ph] 1 Apr 2016

I. INTRODUCTION

In quantum technology, it is very common to summarize the results of a reconstruction technique, either full quantum tomography [1–4] or some partial reconstruction scheme [5–10], by the use of fidelity [11, 12]. Once the information about the state of a system has been extracted from a set of experimental data, the fidelity between the reconstructed state and a given target state, is calculated. Fidelity is bounded to the interval $[0,1]$. High values such as 0.9 or 0.99 are thus considered as a piece of evidence in order to certify that the reconstructed and the target states i) are very close each other in the Hilbert space, ii) they share nearly identical physical properties. In this framework, quantum resources of the prepared state are often benchmarked with those of the target one, e.g. to assess the performances of a teleportation scheme [13, 14].

The two statements above may appear rather intuitive, with the second one following from the first one. On the other hand, it has been suggested that the use of fidelity may be misleading in several situations involving either discrete or continuous variable systems [15–18]. The main goal of the present paper is to experimentally confirm the first statement and, at the same time, to provide neat examples where the second one is clearly proved wrong.

Given two quantum states described by density matrices $\hat{\rho}_1$ and $\hat{\rho}_2$, the fidelity between them is defined as [11]

$$F(\hat{\rho}_1,\hat{\rho}_2) = \mathrm{Tr}\left[\sqrt{\sqrt{\hat{\rho}_1}\hat{\rho}_2\sqrt{\hat{\rho}_1}}\right]^2 . \tag{1}$$

Fidelity is not a proper distance in the Hilbert space. However, it can be easily linked to a distance, and in turn to a metric over the manifold of density matrices. In fact, the Bures distance between two states is defined as

$$D_B(\hat{\rho}_1,\hat{\rho}_2) = \sqrt{2[1-\sqrt{F(\hat{\rho}_1,\hat{\rho}_2)}]}\,.$$

Fidelity also provides an upper and a lower bound to the trace distance, namely [12]:

$$1-\sqrt{F(\hat{\rho}_1,\hat{\rho}_2)} \leq \frac{1}{2}||\hat{\rho}_1-\hat{\rho}_2||_1 \leq \sqrt{1-F(\hat{\rho}_1,\hat{\rho}_2)}\,.$$

These relationships ensure that higher values of fidelity correspond to geometrical proximity of the two states in the Hilbert space. However, they do not seem straightforwardly related to the physical properties of the two states. In turn, it has been pointed out [15–18] that a pair of states that appear very close to each other in terms of fidelity, may be very far in terms of physical resources. Relevant examples may be found with bipartite systems of either qubits or CV Gaussian states, where pairs of states composed by one entangled and one separable states may have (very) high value of fidelity one to each other. Besides, for single-mode CV states high values of fidelity may be achieved by pairs including one state with a classical analogue and a genuinely quantum state of the field.

In this paper, we address the problem experimentally and analyze in details the significance of fidelity as a figure of merit to assess the properties of tomographycally reconstructed state. We address both discrete and continuous variable systems using quantum homodyne tomography to reconstruct CV states and maximum-likelihood polarization tomography for DV ones. In particular, we experimentally address two relevant examples: i) the reconstruction of squeezed thermal states of a single-mode radiation field, analyzing in details the quantum-to-classical transition; and ii) the reconstruction of noisy Werner states of a two-qubit polarization system, inspecting the amount of non-classical correlations. Our results clearly show that high values of fidelity, despite well quantifying geometrical closeness between states in the Hilbert space, may be obtained for quantum states displaying very different physical properties, e.g. quantum resources.

The paper is structured as follows. Sect. II is devoted to continuous variables: we first describe the experimental generation of single-mode squeezed thermal states using a seeded optical amplifier, as well as the homodyne technique employed for tomography. We then present experimental results, illustrating in details the significance of the fidelity of the reconstructed state to a target one and its non-classicality. In Sect. III we illustrate the experimental setup for generating two-qubit states of Werner type and the method of maximum-likelihood estimation for tomography. We then present experimental results, analysing the significance of fidelity of the

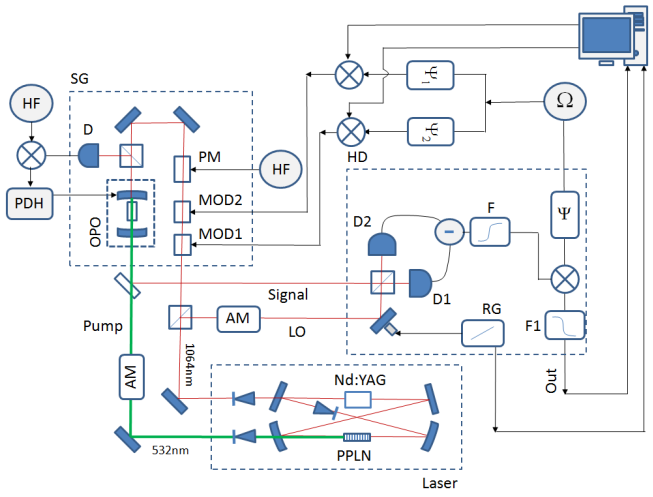

(a)

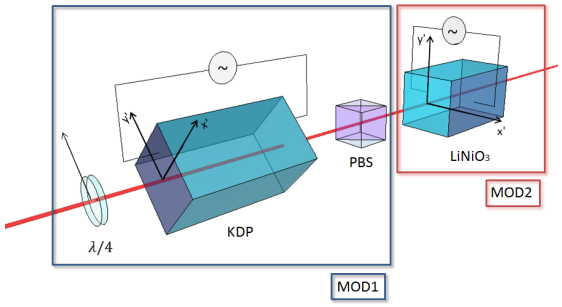

(b)

FIG. 1: (Color online) (a) Schematic diagram of the experimental setup to generate squeezed thermal states. See text for details. (b) Enlarged picture of the optical systems MOD1 and MOD2, used to generate the OPO input signals. The optical field is prepared with circular polarization by setting the fast axis of $\lambda/4$ at an angle of 45° with respect to the incident p-polarization, and then is passed through a KDP crystal whose axis are oriented at 45°. The PBS select only the horizontal component of output beam which is sent in a $LiNiO_3$ crystal whose extraordinary axis is horizontal.

reconstructed states to the target Werner ones in assessing their non-classical correlations, either entanglement or quantum discord. Sect. IV closes the paper with some concluding remarks.

II. SINGLE-MODE GAUSSIAN STATES

In this section we deal with the generation and the characterization of squeezed thermal states (STS) of a single-mode radiation field, i.e. states of the form

$$\hat{\rho} = \hat{S}(r)\hat{\nu}(n_{\rm th})\hat{S}^{\dagger}(r)\,, \tag{2}$$

where $\hat{S}(r) = \exp\left\{\frac{1}{2}r\left[(\hat{a}^{\dagger})^2 - \hat{a}^2\right]\right\}$ is the squeezing operator, with $r \in \mathbb{R}$, $\hat{\nu}(n_{\rm th}) = n_{\rm th}^{\hat{a}^{\dagger}\hat{a}}/(1+n_{\rm th})^{\hat{a}^{\dagger}\hat{a}+1}$ is a thermal state with $n_{\rm th}$ average number of photons and $[\hat{a},\hat{a}^{\dagger}] = 1$, $\hat{a}$ and $\hat{a}^{\dagger}$ being field operators. Upon defining the quadrature operators

$$\hat{x}_{\theta} \equiv \hat{a}\,{\rm e}^{-i\theta} + \hat{a}^{\dagger}\,{\rm e}^{i\theta}\,, \tag{3}$$

with $\theta \in [0,\pi]$, the STS are fully characterized by their first and second moments

$$\langle \hat{x}_{\theta}\rangle = 0 \qquad \forall\theta \tag{4a}$$

$$\langle \Delta\hat{x}_{\theta}^2\rangle = (1+2n_{\rm th})({\rm e}^{2r}\cos^2\theta + {\rm e}^{-2r}\sin^2\theta)\,, \tag{4b}$$

where $\langle\cdots\rangle \equiv {\rm Tr}[\hat{\rho}\cdots]$. In terms of the canonical operators $\hat{x} \equiv \hat{x}_0$ and $\hat{p} \equiv \hat{x}_{\pi/2}$, the covariance matrix (CM) of a STS reads

$$\sigma = \begin{pmatrix} \langle\Delta\hat{x}^2\rangle & 0 \\ 0 & \langle\Delta\hat{p}^2\rangle \end{pmatrix} = \begin{pmatrix} s/\mu & 0 \\ 0 & 1/\mu s \end{pmatrix}, \tag{5}$$

where $\mu = {\rm Tr}[\hat{\rho}^2] = (2n_{\rm th}+1)^{-1}$ is the purity of the state $\hat{\rho}$ and $s \equiv {\rm e}^{2r}$ is the squeezing factor. A STS is nonclassical, i.e. it corresponds to a singular Glauber P-function, whenever the conditions $s < \mu$ or $s > \mu^{-1}$ are satisfied. The total energy of a STS is given by

$$N_{\rm tot} = \langle\hat{a}^{\dagger}\hat{a}\rangle = n_{\rm th} + n_{\rm s} + 2n_{\rm th}n_{\rm s} \quad , \tag{6}$$

where $n_s = \sinh^2 r$ is the number of squeezing photons and $n_{\rm th}$ is the thermal contribution to energy.

According to Eq. (6), it is possible to find a suitable parametrization of the single-mode STS CM (5) in terms of the different energy contributions

$$\langle\Delta\hat{x}^2\rangle = \left(1+2\frac{N_{\rm tot}-n_{\rm s}}{2n_{\rm s}+1}\right)(1+2n_s-2\sqrt{n_{\rm s}+n_{\rm s}^2}) \tag{7a}$$

$$\langle\Delta\hat{p}^2\rangle = \left(1+2\frac{N_{\rm tot}-n_{\rm s}}{2n_{\rm s}+1}\right)\frac{1}{(1+2n_{\rm s}-2\sqrt{n_{\rm s}+n_{\rm s}^2})}, \tag{7b}$$

from which the linear behavior of the variances as a function of the total energy $N_{\rm tot}$ is apparent.

The fidelity between two STS is given by [19]

$$F(\sigma_1,\sigma_2) = \frac{1}{\sqrt{\Delta+\delta}-\sqrt{\delta}}, \tag{8}$$

where $\Delta = \frac{1}{4}\det[\sigma_1+\sigma_2]$ and $\delta = \frac{1}{4}\prod_{i=1,2}(\det\sigma_i - 1)$.

A. Experimental setup

In order to generate STS we employ the experimental setup schematically depicted in Fig. 1 (a). It consists of three stages: Laser, signal generator (SG) and homodyne detector (HD). Our source is a home-made internally frequency doubled Nd:YAG laser. It is based on a 4 mirrors ring cavity and the active medium is a cylindrical Nd:YAG crystal (diameter 2 mm and length 60 mm) radially pumped by three array of water-cooled laser diodes @ 808 nm. The crystal for the frequency doubling is a periodically poled $MgO:LiNbO_3$ (PPLN) of 10 mm thermally stabilized (∼70°C). Inside the cavity is placed a light diode that consist of a half-wave-plate

TABLE I: Characterization, via homodyne tomography, of the $m = 14$ experimental STS in terms of the position and momentum variances, total energy, squeezing factor and purity. The STS display squeezing in position and anti-squeezing in momentum coordinates ($r < 0$) .

state #	$\langle\Delta\hat{x}^2\rangle$	$\langle\Delta\hat{p}^2\rangle$	$\langle\hat{a}^\dagger\hat{a}\rangle$	$s_{\rm exp}$	$\mu_{\rm exp}$
1	0.48 ± 0.03	3.15 ± 0.09	0.41 ± 0.02	0.39 ± 0.01	0.81 ± 0.03
2	0.67 ± 0.04	3.33 ± 0.09	0.50 ± 0.02	0.45 ± 0.01	0.67 ± 0.02
3	0.62 ± 0.04	3.77 ± 0.11	0.60 ± 0.02	0.40 ± 0.02	0.66 ± 0.02
4	0.69 ± 0.05	3.94 ± 0.11	0.66 ± 0.02	0.41 ± 0.02	0.61 ± 0.02
5	0.70 ± 0.05	4.51 ± 0.12	0.80 ± 0.03	0.39 ± 0.02	0.56 ± 0.02
6	0.77 ± 0.05	4.54 ± 0.13	0.83 ± 0.03	0.41 ± 0.02	0.54 ± 0.02
7	0.77 ± 0.05	4.60 ± 0.13	0.84 ± 0.03	0.41 ± 0.02	0.53 ± 0.02
8	0.93 ± 0.06	5.00 ± 0.14	0.98 ± 0.03	0.43 ± 0.02	0.46 ± 0.02
9	0.95 ± 0.06	5.36 ± 0.15	1.08 ± 0.03	0.42 ± 0.01	0.44 ± 0.02
10	0.93 ± 0.07	5.56 ± 0.15	1.12 ± 0.03	0.41 ± 0.02	0.44 ± 0.02
11	1.00 ± 0.07	5.80 ± 0.17	1.20 ± 0.03	0.42 ± 0.02	0.42 ± 0.02
12	1.13 ± 0.07	5.87 ± 0.16	1.25 ± 0.03	0.44 ± 0.02	0.39 ± 0.01
13	1.11 ± 0.08	6.33 ± 0.18	1.36 ± 0.04	0.42 ± 0.02	0.38 ± 0.01
14	1.30 ± 0.08	6.16 ± 0.18	1.36 ± 0.04	0.46 ± 0.02	0.35 ± 0.01

(HWP), a Faraday rotator (15°) and a Brewster plate (BP) in order to obtain the single mode operation.

The laser output @ 532 nm is used as the pump for a optical parametric oscillator (OPO) while the output at 1064 nm is split into two beams by using a polarizing beam splitter (PBS): one is used as the local oscillator (LO) for the homodyne detector and the other as the input for the OPO. The OPO cavity is linear with a free spectral range (FSR) of 3300 MHz, the output mirror has a reflectivity of 92% and the rear mirror 99%. A phase modulator (PM) generate a signal at frequency of 110 MHz (HF) used as active stabilization of the OPO cavity via the Pound-Drever-Hole (PDH) technique [20, 21]: the reflected beam from cavity is detected (D) and used to generate the error signal of PDH apparatus. This signal error drives a piezo connected to the rear mirror of the OPO cavity to actively control its length.

The homodyne detector (HD) consists of a 50:50 beam splitter, two low noise detector and a differential amplifier based on a LMH6624 operational amplifier. The visibility of the interferometer is about 98%. To remove the low frequency signal we use an high-pass filter @ 500 kHz and then the signal is sent to the demodulation apparatus. The information about the signal, that is at frequency Ω about 3MHz, is retrieved by using an electronic apparatus which consists of a phase shifter a mixer and a low pass filter @ 300 kHz. The LO phase is spanned between 0 and 2π thanks to a piezo-mounted mirror linearly driven by a ramp generator (RG).

Our goal is to study a single-mode squeezed thermal state and therefore we have to generate a thermal seed to be injected into the OPO. The density matrix of thermal state in the Glauber representation reads as follows

$$\hat{\nu}_{\rm exp}(n_{\rm th}) = \int_0^\infty d|\alpha|\frac{2|\alpha|}{n_{\rm th}}e^{-\frac{|\alpha|^2}{n_{\rm th}}}\int_0^{2\pi}\frac{d\phi}{2\pi}||\alpha|e^{i\phi}\rangle\langle|\alpha|e^{i\phi}|\,, \tag{9}$$

i.e., it can be viewed as a mixture of coherent states with phase ϕ uniformly distributed over the range 0 to 2π, and a given amplitude $|\alpha|$ distribution. Therefore, we have to generate a rapid sequence of coherent states with $|\alpha|$ and ϕ randomly selected from these distributions.

Our strategy is to exploit the combined effect of the two optical systems (MOD1 and MOD2 in Fig. 1 (a) described in Ref. [22] and sketched in more detail in Fig. 1 (b). MOD1 generate a coherent state with phase 0, while MOD2 generate a coherent state with phase $\frac{\pi}{2}$. By matching these coherent states with properly chosen amplitudes, it is possible to generate an arbitrary coherent state. In order to control this process via pc, the MOD1 and MOD2 are driven by two identical electronic circuits which consist of a phase shifter and a mixer. The pc processes the $|\alpha|$ and ϕ values of the coherent state which we want to generate, and convert them into the voltage signals which are sent to the mixer together with the sinusoidally varying signals at frequency Ω in order to obtain the right modulation signals on MOD1 and MOD2.

Finally, in order to obtain the desired thermal state, the pc generates random $|\alpha|$ and ϕ values according to their specified distributions (see Eq. (9)) and converts them in two simultaneous trains of voltage values which are sent to the crystals in a time window of 70 ms with a repetition rate of 100 kHz. Generation and acquisition operations are synchronized in the same time window at the same sampling rate. Therefore we collect 7000 homodyne data points $\{(\theta_k, x_k)\}$, LO phase and quadrature value, respectively. The sampling is triggered by

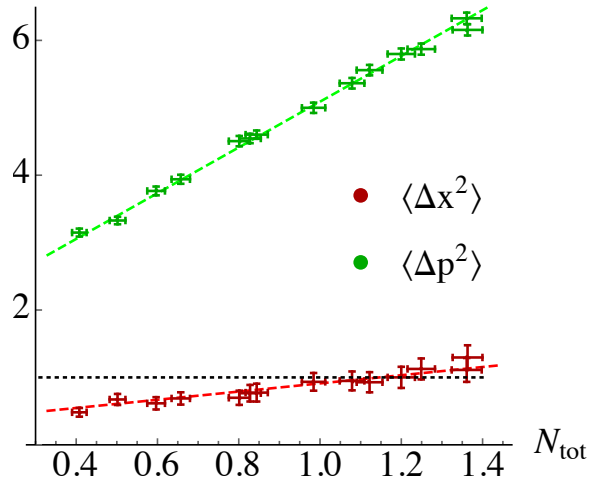

FIG. 2: (Color online) Tomographic reconstruction of the variances of the squeezed quadrature $\hat{x}$ (red dots) and of the anti-squeezed quadrature $\hat{p}$ (green dots) as a function of the total energy $N_{\rm tot}$, for $m = 14$ experimental STS. Dashed lines represent linear fits of the experimental data (see Eqs. (7)), from which we obtain the number of squeezed photons $n_{\rm s} \simeq 0.2$. The black dotted horizontal line is the shot-noise level at $\langle \Delta\hat{x}^2 \rangle = \langle \Delta\hat{p}^2 \rangle = 1$.

a signal generated by RG to ensure the synchronization between the acquisition process and the scanning of LO with $\theta_k \in [0, 2\pi]$.

Notice that seeding the OPO is a crucial step to observe the quantum-to-classical transition with STS. As a matter of fact, without seeding the OPO, output signal is a squeezed vacuum state, which is then degraded to a STS with a nonzero thermal component by propagation in a lossy channel. However, STS obtained in this way are always non-classical for any value of the loss and the squeezing parameters [23–25].

B. Homodyne Tomography

We perform state reconstruction of single-mode CV systems by quantum homodyne tomography, i.e. by collecting homodyne data at different LO phases and applying the pattern functions method [1]. This technique allows one to obtain the expectation value of any observable $\hat{O}$ on a given state $\hat{\rho}$ starting from a set of homodyne data $\{(\theta_k, x_k)\}$, x_k being the k-th outcome from the measurement of the quadrature (3) at phase θ_k, with $k = 1, \ldots, M$. Upon exploiting the Glauber representation of operators in polar coordinates, the average value of a generic observable $\hat{O}$ may be rewritten as

$$\langle \hat{O} \rangle = \int_0^{\pi} \frac{d\theta}{\pi} \int_{-\infty}^{+\infty} dx\, p(x,\theta) \mathscr{R}[\hat{O}](x,\theta), \qquad (10)$$

where $p(x,\theta) = \langle x_\theta | \hat{\rho} | x_\theta \rangle$ is the distribution of quadrature outcomes, with $\{|x_\theta\rangle\}$ the set of eigenvectors of $\hat{x}_\theta$, and $\mathscr{R}[\hat{O}](x,\theta) = \int_{-\infty}^{+\infty} dy |y| \mathrm{Tr}[\hat{O} e^{iy(\hat{x}_\theta - x)}]$ is the estimator of the operator ensemble average $\langle \hat{O} \rangle$. For large samples $M \gg 1$, the integral (10) can be recast in the discrete form

$$\langle \hat{O} \rangle \simeq \frac{1}{M} \sum_{k=1}^{M} \mathscr{R}[\hat{O}](x_k, \theta_k). \qquad (11)$$

The uncertainty of the estimated value $\langle \hat{O} \rangle$ is ruled by the central limit theorem and scales as $\sqrt{M}$, namely

$$\delta\langle \hat{O} \rangle = \frac{1}{\sqrt{M}} \sqrt{\sum_{k=1}^{M} \frac{\left[\mathscr{R}[\hat{O}](x_k,\theta_k)\right]^2 - \langle \hat{O} \rangle^2}{M}}. \qquad (12)$$

In order to properly characterize a single-mode prepared in a Gaussian STS, we need to estimate the first two moments of the quadrature operator $\hat{x}_\phi$ and reconstruct the first-moment vector and the CM, as well as the total energy $\hat{a}^\dagger \hat{a}$ of the state. We thus need the following estimators [1]:

$$\mathscr{R}[\hat{x}_\phi](x,\theta) = 2x\cos(\theta - \phi) \qquad (13a)$$

$$\mathscr{R}[\hat{x}_\phi^2](x,\theta) = (x^2 - 1)\Big\{1 + 2\cos[2(\theta - \phi)]\Big\} + 1 \qquad (13b)$$

$$\mathscr{R}[\hat{a}^\dagger \hat{a}](x,\theta) = \frac{1}{2}\left(x^2 - 1\right). \qquad (13c)$$

In this way it is possible to compute the average value $\langle \hat{O} \rangle$ and the fluctuations $\langle \Delta\hat{O}^2 \rangle \equiv \langle \hat{O}^2 \rangle - \langle \hat{O} \rangle^2$ for the observables of interest, toghether with the corresponding uncertainties (12).

We collect $M = 7000$ homodyne data $\{(x_k, \theta_k)\}$ for each state and address the quantum-to-classical transition by generating $m = 14$ STS with increasing thermal component, as the squeezing is fixed by the geometry of the experimental setup. For all the generated states, we tested the compatibility with the typical form of the STS, i. e. null first-moment vector (4a) and diagonal CM (5). We characterized these states (see Table I) in terms of the position $\langle \Delta\hat{x}^2 \rangle$ and momentum $\langle \Delta\hat{p}^2 \rangle$ variances, the total energy $N_{\rm tot} \equiv \langle \hat{a}^\dagger \hat{a} \rangle$, together with the squeezing factor $s_{\rm exp}$ and the purity $\mu_{\rm exp}$. As already mentioned at the beginning of this section, the shot-noise threshold is set at $\langle \Delta\hat{x}^2 \rangle = \langle \Delta\hat{p}^2 \rangle = 1$, under which the state of the detected single-mode radiation displays genuine quantum squeezing. The generated STS display squeezing in position quadrature and anti-squeezing in momentum quadrature (i.e. we have real and negative squezing parameter $r < 0$). In Fig. 2 we show the position and momentum variances as a function of the total energy for the $m = 14$ experimentally generated STS. A linear fitting, following Eq. (7), provides the value of the number of squeezed photons $n_{\rm s} \simeq 0.2$, which corresponds to ~ 3.7 dB of squeezing. Figure 2 makes apparent the capability of the experimental setup to generate STS-on-demand by seeding the OPO with a controlled number of thermal photons and in turn, to monitor the quantum-to-classical transition of a single-mode Gaussian state of light.

C. Fidelity

In order to perform the uncertainties budget, to discuss the statistical distribution of relevant quantities, and to assess

the statistical significance of fidelity, we generate $N_{\rm MC} = 10^3$ Monte Carlo replica data samples (see Appendix A), for each experimental state. Resampled (raw) homodyne data are drawn from Gaussian distributions using the experimental values of Table I to build the average values (4a) and the variances (4b) of the distributions. For all the $m = 14$ STS we apply homodyne tomography and analyze the distribution of the reconstructed states in the neighbouring of the experimental target state. Results are shown in Fig. 3 and Fig. 4. using the squeezing-purity plane-$\{s,\mu\}$ representation. Figure 3 focuses on three specific states (number 7, 9 and 13 of Table I) which are closer to the quantum-classical boundary. Target states correspond to black points whereas the ovoidal regions denotes the set of states having fidelity larger than $F > 0.995$ to the target. The darker, stripe-like, regions within each balloon correspond to states satisfying the additional constraint of having fluctuations of the total energy (6) at most within one standard deviation.

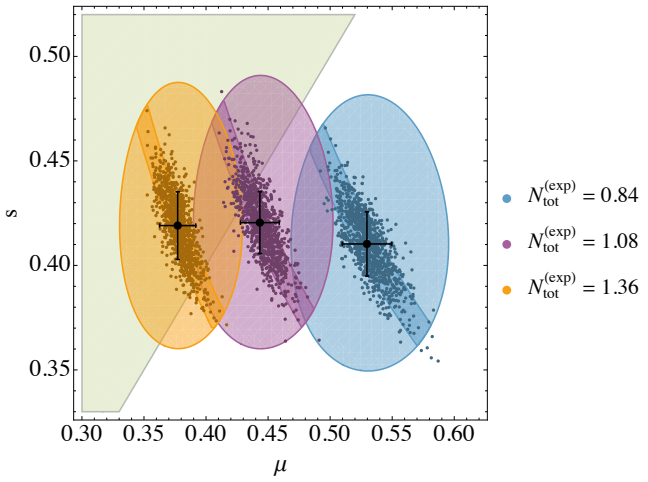

FIG. 3: (Color Online) Statistical distribution of reconstructed STS in the squeezing-purity plane-$\{s,\mu\}$. Data come from $N_{\rm MC}$ Monte Carlo resampled set of data for STS (see text and Appendix A). From left to right, we have distributions for three experimental STS (state number 7,9 and 13 of Table I), shown as black points with the corresponding bars of precision. The triangular-like region $s > \mu$ contains states with a classical analogue. The whole set of reconstructed states are contained in the ovoidal regions, i.e. have fidelity $F > 0.995$ to the corresponding target state. The stripe-like regions are obtained adding a constraint to the total energy, i.e. $N_{\rm tot}^{(\rm exp)} - \delta N_{\rm tot}^{(\rm exp)} < \langle \hat{a}^\dagger \hat{a} \rangle < N_{\rm tot}^{(\rm exp)} + \delta N_{\rm tot}^{(\rm exp)}$.

As it is apparent from the plot, the distribution of STS is concentrated within those stripes. On the other hand, despite the distributions are very sharp in terms of fidelity to their targets (remind that the balloons contains states with fidelity larger than $F \geq 0.995$ to the target), their physical properties may be very different. This fact is clearly illustrated looking at nonclassicality, i.e. checking whether the Glauber P-function of the state is regular (this happens if $s > \mu$, corresponding to a triangular region in Fig. 3) or singular: states with very high fidelity to a classical or a nonclassical target may not share this property with the target itself.

This effect may be not particularly surprising for target states at border of the classicality region, even for high values of fidelity. On the other hand, the point becomes far more relevant if values of fidelity commonly used in experiments are considered. In Fig. 4 we show the balloons of states having fidelity $F \geq 0.9$ or $F \geq 0.95$ to a nonclassical target STS. As it is apparent from the plot, *all* the generated STS are contained in the ballons, irrespectively of their nonclassicality. The compatibility region may be considerably reduced in size by adding an energy constraint but, nonetheless, a large number of states may still fall in the region of classicality.

Overall, we conclude that fidelity is not a significant figure of merit to assess nonclassicality of STS and should not be employed to benchmark a generation scheme or certify quantum resources for a given protocol.

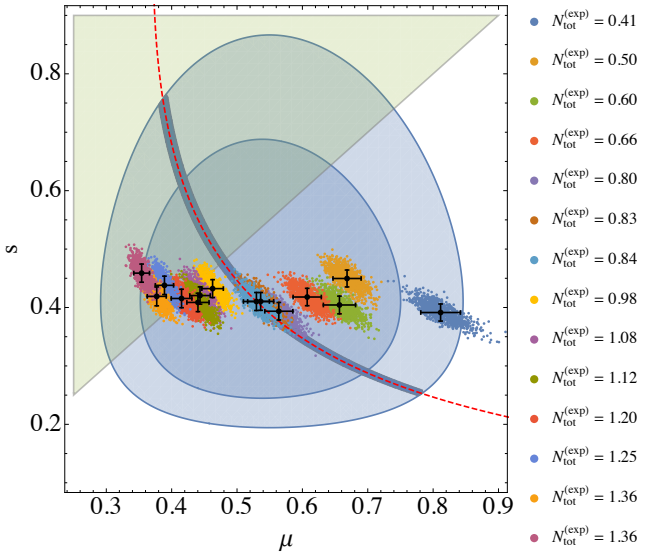
0.8
0.6
0.4
0.2
s
0.3 0.4 0.5 0.6 0.7 0.8 0.9
μ
$N_{\rm tot}^{(\rm exp)} = 0.41$
$N_{\rm tot}^{(\rm exp)} = 0.50$
$N_{\rm tot}^{(\rm exp)} = 0.60$
$N_{\rm tot}^{(\rm exp)} = 0.66$
$N_{\rm tot}^{(\rm exp)} = 0.80$
$N_{\rm tot}^{(\rm exp)} = 0.83$
$N_{\rm tot}^{(\rm exp)} = 0.84$
$N_{\rm tot}^{(\rm exp)} = 0.98$
$N_{\rm tot}^{(\rm exp)} = 1.08$
$N_{\rm tot}^{(\rm exp)} = 1.12$
$N_{\rm tot}^{(\rm exp)} = 1.20$
$N_{\rm tot}^{(\rm exp)} = 1.25$
$N_{\rm tot}^{(\rm exp)} = 1.36$
$N_{\rm tot}^{(\rm exp)} = 1.36$

FIG. 4: (Color online) Statistical distribution of reconstructed STS in the squeezing-purity plane-$\{s,\mu\}$ for all the experimental target states in Table I (black points). The two balloons include states having fidelity to a nonclassical target STS (with $s = 0.41$ and $\mu = 0.53$) larger than $F > 0.90$ (outer balloon) or $F > 0.95$ (inner balloon) respectively, i.e. values commonly recognized as regions of *high fidelity*. The size of the compatibility regions may be reduced by adding energy constraints (as discussed in Fig. 3). A significant amount of states may still display opposite classicality properties compared to the target.

III. TWO-QUBIT SYSTEMS

In this Section we deal with discrete two-qubit systems. In particular we focus on two-photon polarization states $|HH\rangle$, $|HV\rangle$, $|VH\rangle$ and $|VV\rangle$, and address the reconstruction of statistical mixtures belonging to the class of Werner states:

$$\hat{\rho}^{(w)} = p\,|\Psi^-\rangle\langle\Psi^-| + \frac{1-p}{4}\hat{\mathbb{I}}_4, \qquad (14)$$

where $\hat{\mathbb{I}}_4$ is the identity operator in the 4-dimensional Hilbert space of two qubits and $|\Psi^-\rangle$ is one of the maximally entan-

gled Bell states

$$|\Phi^{\pm}\rangle = \frac{|HH\rangle \pm |VV\rangle}{\sqrt{2}} \quad \text{and} \quad |\Psi^{\pm}\rangle = \frac{|HV\rangle \pm |VH\rangle}{\sqrt{2}}. \quad (15)$$

The parameter $-1/3 \leq p \leq 1$ tunes the mixture (14) from the maximally mixed state $\hat{\mathbb{I}}_4/4$ for $p = 0$ to the maximally entangled Bell state $|\Psi^-\rangle$ for $p = 1$. In between, the quantum-to-classical transition is located at $p = 1/3$, with entangled states satisfying $p > 1/3$ and separable ones $p < 1/3$.

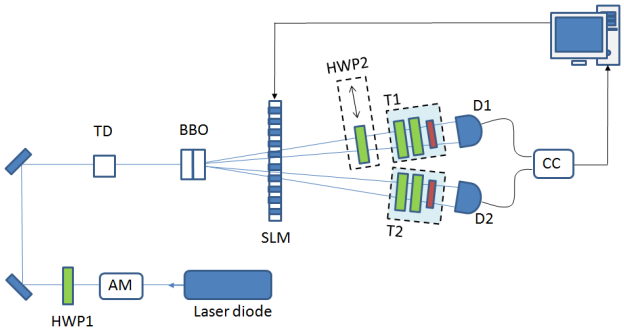

FIG. 5: (Color online) Schematic diagram of experimental setup. A linearly polarized cw laser diode at 405 nm pumps a couple of BBO crystals cut for type-I downconversion. The horizontal and vertical amplitudes of the photon pairs are balanced by a half-wave plate set along the pump path (HWP1), whereas an additional BBO crystal (TD) is placed on the pump path to compensate the temporal delay. The amplitude modulator (AM) consists of a half-wave-plate and polarizer-beam-splitter. Signal and idler beams travel through the SLM, which provides purification of the generated states. A half-wave plate (HWP2) is inserted on signal path in order to generate the state $\hat{\rho}_\lambda$ (see the text), whereas a quarter-wave plate, a half-wave plate, and a polarizer (sectors T1 and T2) are used for the tomographic reconstruction. Finally the beams are detected by detectors D1 and D2 ad sent to single-photon counting modules (CC)

A. Experimental generation of Werner states

A schematic diagram of experimental setup is sketched in Fig. 5. Photon pairs are generated by type-I downconversion from a couple of beta barium borate (BBO) crystals, in a non-collinear configuration, pumped with a linearly polarized cw 405 nm laser diode, whose effective power on the generating crystals is about 10 mW. The experimental apparatus has been already described in detail in Refs. [26, 27]. Here a half-wave plate (HWP2 in Fig. 5) has been inserted in front of detector D1 to perform $|\Phi^-\rangle \to |\Psi^-\rangle$ transformation. A programmable one-dimensional spatial light modulator (SLM) is placed on the path of signal and idler in order to control the visibility of the generated states. The SLM provides the setup with great flexibility, allowing the experimenter to choose and set the visibility of generated states [28, 29]. Eventually, photons are focused in two multimode fibers and sent to single-photon counting modules (CC).

Our experimental apparatus allows us to mix two types of Bell states at a time, either $|\Psi^{\pm}\rangle$ or $|\Phi^{\pm}\rangle$. In order to obtain a Werner state (14) we generate the polarization entangled states $\hat{\rho}_\lambda = \lambda|\Psi^-\rangle\langle\Psi^-| + (1-\lambda)|\Psi^+\rangle\langle\Psi^+|$ and the mixed state $\hat{\rho}_{\rm mix} = (|\Phi^+\rangle\langle\Phi^+| + |\Phi^-\rangle\langle\Phi^-|)/2$ [26, 30]. Werner states may be obtained by suitably mixing these two states $\hat{\rho}^{(w)} = f_1\hat{\rho}_\lambda + f_2\hat{\rho}_{\rm mix}$ with proper probabilities, given by $f_1 = \frac{1+p}{2}$, $f_2 = \frac{1-p}{2}$ and $\lambda = \frac{2p}{p+1}$. The mixed state $\hat{\rho}_{\rm mix}$ is obtained using the same scheme of Fig. 5 upon removing the HWP2 from the signal path and setting the SLM in order to get $\lambda \simeq 0$. The frequencies f_1 and f_2 are tuned by changing the power of the pump beam with an amplitude modulator (AM). The full range of Werner states may be explored.

The tomographic reconstruction is performed by measuring 16 projective and independent observables in the two-qubit Hilbert space, namely $P_j = |\psi_j\rangle\langle\psi_j|$ (with $j = 1,\ldots,16$). Different settings of the apparatus, obtained by combining a quarter-wave plate, a half-wave plate and a polarizer (sectors T1 and T2 in Fig. 5), are employed [31, 32]. Each of the 16 measurements correspond to 30 acquisitions, in a time window of 1 s, of coincidence photon counts $\{n_j\}_{j=1}^{16}$, i.e. the outcomes of the projectors P_j.

B. Tomography with MLE

The density matrix of the two-qubit states generated in the experiment has been reconstructed using maximum-likelihood (MLE) tomographic protocol [31, 32]. This scheme adopts a suitable parametrization of the density matrix, namely $\hat{\rho}(\mathbb{T}) = T^\dagger T/{\rm Tr}[T^\dagger T]$, where T is a complex lower triangular matrix and $\mathbb{T} = \{t_j\}_{j=1}^{16}$ is the set of 16 parameters characterizing the density matrix. In this way it is ensured that $\hat{\rho}$ is positive and Hermitean (Choleski decomposition). The MLE protocol allows to recover the set $\mathbb{T}$ by means of a constrained optimization procedure with Lagrange multipliers, which accounts for the normalization condition ${\rm Tr}[\hat{\rho}] = 1$, involving the set of data coming from the 16 experimental measurements. In particular, the logarithmic likelihood functional to be minimized reads

$$\mathscr{L}(\mathbb{T}) = \sum_{j=1}^{16} \frac{[\mathscr{N}\langle\psi_j|\hat{\rho}(\mathbb{T})|\psi_j\rangle - n_j]^2}{2\mathscr{N}\langle\psi_j|\hat{\rho}(\mathbb{T})|\psi_j\rangle}, \quad (16)$$

where $\mathscr{N} = \sum_{j=1}^{4} n_j$ is a constant proportional to the total number of acquisitions.

We experimentally generated $N_{\rm exp} = 4$ two-qubit states not too far from the border between separable and entangled states (see Table II). MLE quantum tomography shows that the reconstructed density matrices do not display the typical X-shape of an ideal Werner state (14) with real-valued elements. A possible route to extract the desired Werner state, is based on the maximization of the fidelity between the experimental state and the generic Werner state (14). This procedure sounds reasonable and, in principle, may allow one to assess the quantum resources contained in the generated state, as well as to exploit them in order to accomplish quantum tasks. On the other hand, we will show in the following that a fidelity-based inference is in general misleading and should be avoided in

TABLE II: Statistical analysis of the tomography of $N_{\rm MC}=10^3$ two-qubit states, having fidelities $F(\overline{\hat{\rho}}_k,\hat{\rho}_k^{(w)})$ with target Werner of parameter $p_k^{(w)}$. The average values of the least eigenvalue $e_m(\hat{\rho}^{(\tau)})$ and of quantum discord $D(\hat{\rho})$ are reported for both the distributions of tomographic states and of the approximated Werner states.

	state 1	state 2	state 3	state 4
$p_k^{(w)}$	0.32 ± 0.04	0.35 ± 0.04	0.28 ± 0.04	0.44 ± 0.05
$F(\overline{\hat{\rho}}_k,\hat{\rho}_k^{(w)})$	$0.985^{+0.006}_{-0.01}$	$0.988^{+0.005}_{-0.01}$	$0.987^{+0.006}_{-0.01}$	$0.985^{+0.007}_{-0.02}$
$e_m(\overline{\hat{\rho}}_k^{(\tau)})$	0.01 ± 0.03	-0.01 ± 0.03	0.04 ± 0.03	-0.07 ± 0.03
$e_m([\hat{\rho}_k^{(w)}]^{(\tau)})$	0.01 ± 0.03	-0.01 ± 0.03	0.04 ± 0.03	-0.08 ± 0.04
$D(\overline{\hat{\rho}}_k)$	0.08 ± 0.02	0.10 ± 0.02	0.06 ± 0.02	0.14 ± 0.02
$D(\hat{\rho}_k^{(w)})$	0.11 ± 0.03	0.14 ± 0.03	0.06 ± 0.02	0.21 ± 0.04

assessing the true quantum properties of the experimentally generated state.

C. Fidelity

In order to perform statistical analysis of data and evaluate uncertainties we have resampled photon counts data to obtain $N_{\rm MC}=10^3$ repeated samples for each of the $N_{\rm exp}=4$ experimental states (see Appendix A for details). The significance of fidelity may be assessed upon the comparison between two possible strategies to reconstruct quantum properties of the generated states and their distribution. In the first strategy we evaluate properties from the reconstructed states $\hat{\rho}_k^i$ ($k=1,\ldots,N_{\rm exp}$ and $i=1,\ldots,N_{\rm MC}$) as obtained by the MLE tomography, whereas in the second one we look for the closest Werner state, in terms of fidelity, for each reconstructed state and analyze the properties of this class of Werner states $[\hat{\rho}_k^i]^{(w)}$.

The first method is based only in tomographic data and provides an average MLE two-qubit state $\overline{\hat{\rho}}_k=\sum_{i=1}^{N_{\rm MC}}\hat{\rho}_k^i/N_{\rm MC}$, which optimize the likelihood of the experimental data. This average state may be then employed to infer a Werner target state $\hat{\rho}_k^{(w)}$, of the form given in Eq. (14), via a maximization of the fidelity $F(\overline{\hat{\rho}}_k,\hat{\rho}_k^{(w)})$. Upon adopting the second strategy, we obtain a distribution of approximated Werner states, with an average state compatible, at least in principle, with the Werner target state of the first strategy. The parameters $p_k^{(w)}$ characterizing the Werner target states are reported in Table II.

In the following, we analyze how some properties of the quantum states distribute around the target states in terms of fidelity, depending on which of the two strategies has been adopted. In particular we consider the amount of quantum correlations of two-qubit states, as quantified by entanglement and quantum discord.

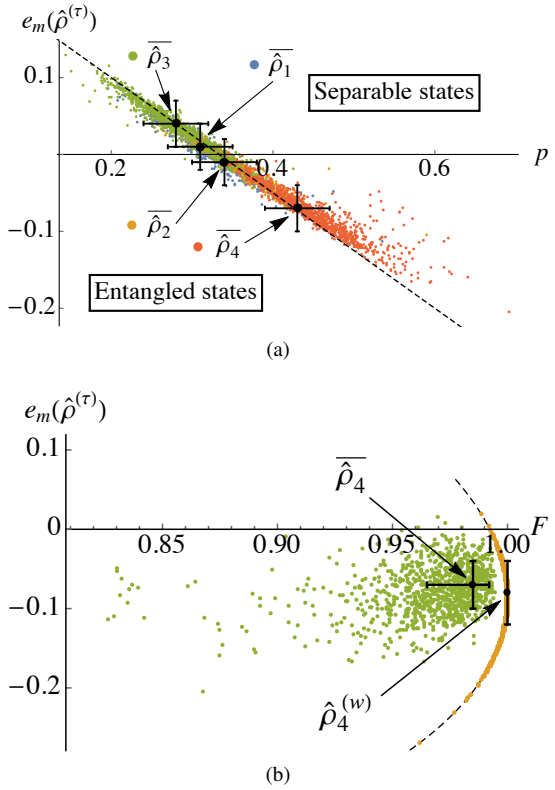

FIG. 6: (Color online) (a) Distribution of $e_m([\hat{\rho}_k^i]^{(\tau)})$ for 10^3 resampled states as a function of the Werner parameter p. The $N_{\rm exp}=4$ average states $\overline{\hat{\rho}}_k$ are highlighted with black dots and error bars, matching the theoretical curve $e_m(\hat{\rho}^{(w)})=(1-3p)/4$ (dashed black line) relative to the negative eigenvalue of the partially transposed ideal Werner state (14). Moreover, it is evident how many states may cross the boundary between entangled and separable states. (b) Distribution of $e_m([\hat{\rho}_4^i]^{(\tau)})$ for 10^3 simulations of the target state $\overline{\hat{\rho}}_4$ as a function of the fidelity $F(\hat{\rho}_4^i,\hat{\rho}_4^{(w)})$ (green dots). The same distribution as a function of $F([\hat{\rho}_4^i]^{(w)},\hat{\rho}_4^{(w)})$ (orange dots), matches with the theoretical parametric curve (dashed black curve) obtained by evaluating F and e_m of the approximated Werner states. The values of entanglement for the average state $\overline{\hat{\rho}}_4$ and for the target Werner state $\hat{\rho}_4^{(w)}$, are compatible (black dots and error bars).

1. Entanglement

The separability of two-qubit systems is established by the Peres-Horodecki criterion [33, 34]: a quantum state of two qubits $\hat{\rho}$ is separable if and only the partially transposed density matrix is positive, i.e. $\hat{\rho}^{(\tau)} \geq 0$. Thus, it is possible to study entanglement or separability properties by evaluating the eigenvalues of the partially transposed density matrix. We compute the minimum of these eigenvalues

$$e_m(\hat{\rho}^{\tau}) \equiv \min\{\lambda_n^{\tau}\}_{n=1}^{4}, \tag{17}$$

for both the considered strategies, i.e. for the distributions of resampled states $\hat{\rho}_k^i$ and of the approximated Werner states $[\hat{\rho}_k^i]^{(w)}$. For a Werner state the minimum eigenvalue, which may assume negative values, is given by $e_m([\hat{\rho}^{(w)}]^{\tau}) = (1-3p)/4$.

In Fig. 6 (a) we plot the distribution of $e_m(\hat{\rho}^{\tau})$ as a function of the Werner parameter p for all the $N_{\mathrm{MC}} = 10^3$ resampled states, with average tomographic states $\overline{\hat{\rho}_k}$. We note that the average states arrange along the curve of the theoretical behavior for a Werner state and that the resampled states follow the same prediction (see Table II). Nonetheless, there is evidence of some states generated from a separable experimental state in the entangled region, and viceversa. This first observation reveals that statistical fluctuations in an experiment may still produce quantum states with properties radically different from the expected ones, such as separability and entanglement. In Fig. 6 (b), we focus on the most entangled state $\overline{\hat{\rho}_4}$ and compare the distribution of the resampled states and of the corresponding Werner states, in terms of $e_m(\hat{\rho}^{\tau})$ and fidelity with the target state $\hat{\rho}_4^{(w)}$. In this way we can highlight the differences between the two possible strategies for data analysis, i.e. between the evaluation of the properties of the direct tomographic states and the approximated Werner states. This second strategy compel the resampled states to follow the single-parameter Werner state (14) and, thus, to force the distribution of the least eigenvalue $e_m([\hat{\rho}_k^{(w)}]^{(\tau)})$ according to the theoretical prediction (dashed black curve in the plot). In this way, we obtain a distribution of Werner states having, obviously, very high values of fidelity with the target (Werner) state. On the other hand, tomographic states display lower values of fidelity with the target state, but $e_m(\hat{\rho}^{\tau})$ is evaluated directly from the tomographic density matrices. From the statistical analysis, we conclude that the estimated value of $e_m(\hat{\rho}^{\tau})$ is compatible within errors for both the adopted strategies. We will see in the following that these two strategies may lead to different and non-compatible results for another property of quantum states, the quantum discord.

2. Quantum discord

Another widely adopted measure of the amount of quantum correlations in a state $\hat{\rho}$ is the quantum discord [35, 36], which is defined starting from two equivalent definitions, in the classical domain, of the mutual information, i.e. the total amount

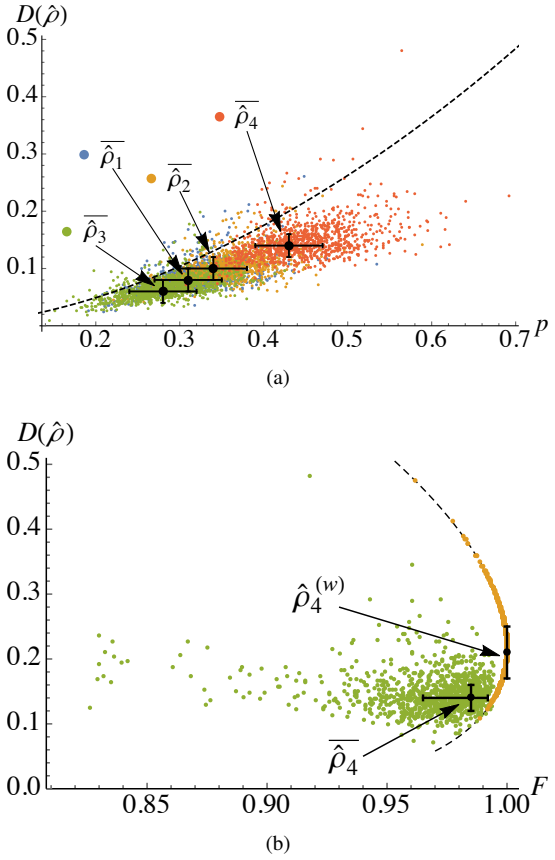

FIG. 7: (Color online) (a) Distribution of $D(\hat{\rho}_k^i)$ for 10^3 resampled states as a function of the Werner parameter p. The $N_{\mathrm{exp}} = 4$ average states $\overline{\hat{\rho}_k}$ are highlighted with black dots and error bars. The theoretical curve $D(\hat{\rho}^{(w)})$ (dashed black line), relative to the discord of the ideal Werner state (14), is systematically higher than the discord distribution of the tomographic states $\hat{\rho}_k^i$. (b) Distribution of $D(\hat{\rho}_4^i)$ for 10^3 simulations of the target state $\overline{\hat{\rho}_4}$ as a function of the fidelity $F(\hat{\rho}_4^i, \hat{\rho}_4^{(w)})$ (green dots). The same distribution as a function of $F([\hat{\rho}_4^i]^{(w)}, \hat{\rho}_4^{(w)})$ (orange dots), matches with the theoretical parametric curve (dashed black curve) obtained by evaluating F and D of the approximated Werner states. The values of quantum discord for the average state $\overline{\hat{\rho}_4}$ and for the target Werner state $\hat{\rho}_4^{(w)}$, are not compatible (black dots and error bars).

of correlations of $\hat{\rho}$:

$$\mathscr{I}(\hat{\rho}) = S(\hat{\rho}_A) + S(\hat{\rho}_B) - S(\hat{\rho}), \tag{18a}$$

$$\mathscr{J}_A(\hat{\rho}) = S(\hat{\rho}_B) - \min \sum_j c_j S(\hat{\rho}_{B|j}), \tag{18b}$$

where $\hat{\rho}_A$ ($\hat{\rho}_B$) is the reduced density matrix of $\hat{\rho}$ for the subsystems A (or B) and $S(\hat{\rho}) = -\mathrm{Tr}[\hat{\rho}\log_2(\hat{\rho})]$ the von Neumann entropy. While the first definition (18a) is based only on the von Neumann entropy, the second one in Eq. (18b) accounts for all the classical correlations that can be detected by local projective measurements only on a subsystem. Here $\hat{\rho}_{B|j} = \mathrm{Tr}_A[\hat{\Pi}_j\hat{\rho}\,\hat{\Pi}_j]/\pi_j$ is the reduced state of B conditioned to the set of projectors $\{\hat{\Pi}_j\}$, with probability $\pi_j = \mathrm{Tr}[\hat{\Pi}_j\hat{\rho}\,\hat{\Pi}_j]$

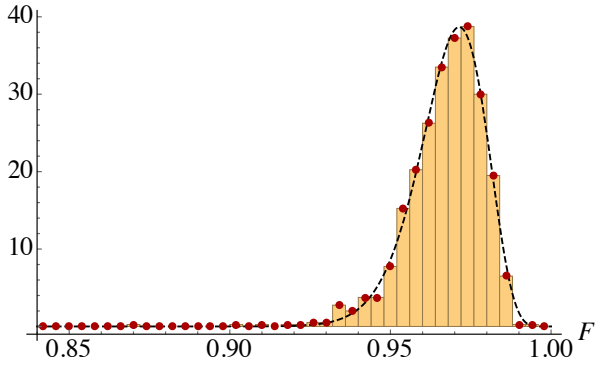

FIG. 8: The histogram shows the distribution of $F(\hat{\rho}_3^i, \hat{\rho}_4^{(w)})$, i.e. the fidelity between a set of separable states and an entangled target state. The data are well fitted by a β-distribution, centered around $F \approx 0.97$.

for the outcome j, and the minimum in Eq. (18b) is taken over all the possible $\{\hat{\Pi}_j\}$. A similar definition applies for local measurements on subsystem B. The quantum discord is then evaluated as the residual information stemming from the difference of the two definitions in Eqs. (18), which has a pure quantum character:

$$D(\hat{\rho}) \equiv \mathscr{I}(\hat{\rho}) - \mathscr{J}_A(\hat{\rho}). \tag{19}$$

For a Werner state (14) the quantum discord can be analytically evaluated:

$$\begin{aligned} D(\hat{\rho}^{(w)}) = &\frac{1+3p}{4}\log_2(1+3p) + \frac{1-p}{4}\log_2(1-p) \\ &- \frac{1+p}{2}\log_2(1+p). \end{aligned} \tag{20}$$

In Fig. 7(a) we plot the quantum discord $D(\hat{\rho}_k^i)$ for all the $N_{\rm MC} = 10^3$ resampled states, with average tomographic states $\overline{\hat{\rho}_k}$, as a function of the Werner parameter p. The theoretical behavior of Eq. (20), represented in the figure by a dashed curve, puts in evidence the high discrepancy with the quantum discord computed for the tomographic states. The approximation to Werner states leads to a systematic over-estimation of the quantum discord for the two-qubit states (see also Table II). We can enforce this result by looking at the distribution of the quantum discord relative to the single set of states $\hat{\rho}_4^i$ only, as a function of the fidelity with the corresponding target Werner state $\hat{\rho}_4^{(w)}$ (see Fig. 7(b)). Most of the states are contained in a region of high values of fidelity, thus suggesting that the approximation to an average Werner state could be correct. Nonetheless, if we consider the distribution of the approximated Werner states, we observe that the values of fidelity increase, but the value of quantum discord of the target Werner state $\hat{\rho}_4^{(w)}$ is out of the limits of compatibility with the average quantum discord $D(\overline{\hat{\rho}_4})$. This suggest that the second strategy employing the approximation to Werner states reveals to be too drastic, as it does not account properly for the actual tomographic reconstruction of the density matrix.

We can conclude that, even though high values of fidelity between a target state and a tomographic state are achieved, the properties of the two can be very different. On an extreme level, we can look at the distribution of the fidelity between the most classical states we generated, $\hat{\rho}_3^i$, and, at the opposite, the most entangled one as the target state, namely $\hat{\rho}_4^{(w)}$. The probability density histogram in Fig. 8 shows that the two kind of states should result compatible with a level of fidelity $F \approx 0.97$, even though they possess clearly different properties.

IV. CONCLUSIONS

In conclusion, we have addressed quantum state reconstruction for DV and CV quantum optical systems and experimentally analyzed the significance of fidelity as a figure of merit to assess the properties of the reconstructed state. State reconstruction, in the two cases, has been performed adopting homodyne and MLE tomography techniques. One of the most natural ways to link the tomographic results to the target states, i.e. the quantum states supposed to be generated by the designed experimental setup, is the evaluation of fidelity. In order to study the relation between fidelity and the experimental states, we performed statistical analysis using Monte Carlo sampling of each experiment, re-generating sets of $N_{\rm MC} = 10^3$ data samples and analyzing the distribution of some of their main properties as a function of fidelity.

In the CV framework, we employed a thermal-state seeded OPO cavity, an experimental configuration which allows to generate STS on-demand. The accurate control of the thermal and squeezing component of the apparatus, allows us to address the quantum-to-classical transition for these states. Our results show that even for high values of fidelity and imposing energy constraints, one may find neighboring states in terms of fidelity which, however, not share the same quantum/classical properties.

In the DV context, we experimentally obtained pairs of polarized photons from type-I downconversion and conveniently generate the Werner mixed states. This one-parameter family of states allowed us to analyze the non-classical properties of two-qubit states in terms of entanglement/separability and to evaluate the amount of quantum correlations by means of the quantum discord. We found that a fidelity based approximation of the tomographic states by Werner states may lead to an overestimation e.g. of the quantum discord. Moreover, high values of fidelity may occur between two very different states in terms of their separability properties.

Overall, we conclude that while fidelity is a good measure of geometrical proximity in the Hilbert space it should not be used as the sole benchmark to certify quantum properties, which should be rather estimated tomographycally in a direct way.

Acknowledgments

This work has been supported by UniMI through the UNIMI14 grant 15-6-3008000-609 and the H2020 Transition Grant 15-6-3008000-625, and by EU through the H2020 Project QuProCS (Grant Agreement 641277).

Appendix A: Evaluation of uncertainties by Monte Carlo resampling

In order to avoid the limitations of finite samples and the influence of systematic unpredictable errors that could be present in an experiment, we evaluate uncertainties by Monte Carlo resampling of data, according to standard metrological prescriptions [37] valid for any statistical models having a single output quantity and input quantities with arbitrary distribution. Here we provide a brief summary of the main assumptions and principles.

The measured quantities of interest X_i are random variables distributed according to a given probability density function (PDF) $\mathscr{G}(X_i)$. In particular, we assume normal distributions characterized by mean value $\langle x_i \rangle$ and standard deviation δx_i. Monte Carlo evaluation of uncertainties is based on sampling random outcomes from $\mathscr{G}(X_i)$ according to experimental data, which themselves fix the the average values and the standard deviations. In particular, as described in the main text, the considered experimental measurements, for CV systems, correspond to homodyne detection of the radiation field quadratures, whereas for DV systems we perform coincidence photon counting measurements of polarized photons. Starting from experimental results, we generate $N_{\rm MC} = 10^3$ resampled replicas of the experiments, thus building a significative sample for the statistical analysis.

[1] G. M. D'Ariano, M. G. A. Paris, and M. F. Sacchi, Adv. Imag. Electr. Phys. **128**, 205 (2003).

[2] M. G. A. Paris and J. Řeháček, *Quantum State Estimation*, Lect. Notes Phys. **649** (2004).

[3] A. I. Lvovsky and M. G. Raymer, Rev. Mod. Phys. **81**, 299 (2009).

[4] C. Schwemmer, L. Knips, D. Richart, H. Weinfurter, T. Moroder, M. Kleinmann, and O. Gühne, Phys. Rev. Lett. **114**, 080403 (2015).

[5] E. T. Jaynes, Phys. Rev. **106**, 620 (1957); *ibidem* **108**, 171 (1957).

[6] V. Bužek, R. Derka, G. Adam, and P.L. Knight Ann. Phys. **266**, 454 (1998).

[7] S. Olivares, and M. G. A. Paris, Phys. Rev. A **76**, 042120 (2007).

[8] G. Zambra, A. Andreoni, M. Bondani, M. Gramegna, M. Genovese, G. Brida, A. Rossi, and M. G. A. Paris, Phys. Rev. Lett. **95**, 063602 (2005).

[9] K. Banaszek, and I. A. Walmsley, Opt. Lett. **28**, 52 (2003).

[10] J. Řeháček, Z. Hradil, O. Haderka, J. Peřina Jr, M. Hamar, Phys. Rev. A **67**, 061801(R) (2003).

[11] A. Uhlmann, Rep. Math. Phys. **9**, 273, (1976).

[12] C. A. Fuchs and J. van de Graaf, IEEE Trans. Inf. Theory **45**, 1216 (1999).

[13] M. Ban, Phys. Rev. A **69**, 054304 (2004).

[14] C. M. Caves, and K. Wodkiewicz, Phys. Rev. Lett. **93**, 040506 (2004).

[15] V. Dodonov, J. Phys. A **45**, 032002 (2012).

[16] M. Bina, A. Mandarino, S. Olivares, and M. G. A. Paris, Phys. Rev. A **89**, 012305 (2014).

[17] A. Mandarino, M. Bina, S. Olivares, and M. G. A. Paris, Int. J. Q. Inf **12**, 1461015 (2014).

[18] C. Benedetti, A. P. Shurupov, M. G. A. Paris, G. Brida, and M. Genovese, Phys. Rev. A **87**, 052136 (2013).

[19] P. Marian, and T. A. Marian, Phys. Rev. A **86**, 022340 (2012).

[20] R. W. P. Drever, J. L. Hall, F. V. Kowalski, J. Hough, G. M. Ford, A. J. Munley, H. Ward, Appl. Phys. B **31**, 97 (1983).

[21] S. Cialdi, C. Porto, D. Cipriani, S. Olivares, M. G. A. Paris, preprint arXiv:1505.03903 [quant-ph], Phys. Rev. A, in press

[22] H. A. Bachor, and T. C. Ralph, *A Guide to Experiments in Quantum Optics* (Wiley-VCH, Weinheim, 2004).

[23] A. R. Rossi, S. Olivares, and M. G. A. Paris, J. Mod. Opt. **51**, 1057 (2004).

[24] A. Ferraro, S. Olivares, and M. G. A. Paris, *Gaussian States in Quantum Information* (Bibliopolis, Napoli, 2005).

[25] S. Olivares, Eur. Phys. J. Special Topics **203**, 3 (2012).

[26] S. Cialdi, F. Castelli, I. Boscolo, and M. G. A. Paris, Appl. Opt. **47**, 1832 (2008).

[27] S. Cialdi, F. Castelli, and M. G. A. Paris, J. Mod. Opt. **56**, 215 (2009).

[28] S. Cialdi, D. Brivio, and M. G. A. Paris, Appl. Phys. Lett. **97**, 041108 (2010).

[29] S. Cialdi, D. Brivio, A. Tabacchini, A. M. Kadhim, and M. G. A. Paris, Opt. Lett. **37**, 3951 (2012).

[30] S. Cialdi, D. Brivio, E. Tesio, and M. G. A. Paris, Phys. Rev. A **84**, 043817 (2011).

[31] K. Banaszek, G. M. D'Ariano, M. G. A. Paris, and M. F. Sacchi, Phys. Rev. A **61**, 010304(R) (1999).

[32] D. F. V. James, P. G. Kwiat, W. J. Munro, and A. G. White, Phys. Rev. A **64**, 052312 (2001).

[33] A. Peres, Phys. Rev. Lett. **77**, 1413 (1996).

[34] M. Horodecki, P. Horodecki, and R. Horodecki, Phys. Lett. A **223**, 1 (1996).

[35] H. Ollivier, and W. H. Zurek, Phys. Rev. Lett. **88**, 017901 (2001).

[36] L. Henderson, and V. Vedral, J. Phys. A **34**, 6899 (2001).

[37] BIPM, IEC, IFCC, ILAC, ISO, IUPAC, IUPAP, and OIML, *Evaluation of Measurement Data - Supplement 1 to the Guide to the Expression of Uncertainty in Measurement - Propagation of Distributions Using a Monte Carlo Method* (JCGM 101, 2008), http://www.bipm.org/utils/common/documents/jcgm/JCGM_101_2008_E.pdf .